

# Cardiac Motion Estimation by Joint Alignment of Tagged MRI Sequences

E. Oubel<sup>a,b</sup>, M. De Craene<sup>a,b</sup>, A. O. Hero<sup>d</sup>, A. Pourmorteza<sup>e</sup>, M. Huguet<sup>f</sup>,  
G. Avegliano<sup>g</sup>, B. H. Bijmens<sup>a,b,c</sup>, A. F. Frangi<sup>a,b,c,\*</sup>

<sup>a</sup>*Center for Computational Imaging & Simulation Technologies in Biomedicine (CISTIB), Information and Communication Technologies Department, Universitat Pompeu Fabra, Barcelona, Spain.*

<sup>b</sup>*Networking Center on Biomedical Research - CIBER-BBN, Barcelona, Spain.*

<sup>c</sup>*Institució Catalana de Recerca i Estudis Avançats, Barcelona, Spain.*

<sup>d</sup>*Department of Electrical Engineering and Computer Science (EECS), The University of Michigan, Ann Arbor, MI, USA.*

<sup>e</sup>*Department of Biomedical Engineering, Johns Hopkins University School of Medicine, Baltimore, MD, USA.*

<sup>f</sup>*Centre Cardiovascular CETIR Sant Jordi, Barcelona, Spain.*

<sup>g</sup>*Instituto Cardiovascular de Buenos Aires (ICBA), Buenos Aires, Argentine.*

---

## Abstract

Image registration has been proposed as an automatic method for recovering cardiac displacement fields from Tagged Magnetic Resonance Imaging (tMRI) sequences. Initially performed as a set of pairwise registrations, these techniques have evolved to the use of 3D+t deformation models, requiring metrics of joint image alignment (JA). However, only linear combinations of cost functions defined with respect to the first frame have been used. In this paper, we have applied  $k$ -Nearest Neighbors Graphs ( $k$ NNG) estimators of the  $\alpha$ -entropy ( $H_\alpha$ ) to measure the joint similarity between frames, and to combine the information provided by different cardiac views in an unified metric. Experiments performed on six subjects showed a significantly higher accuracy ( $p < 0.05$ ) with respect to a standard pairwise alignment (PA) approach in terms of mean positional error and variance with respect to manually placed landmarks. The developed method was used to study strains in patients with myocardial infarction, showing a consistency between strain, infarction location, and coronary occlusion. This paper also presents

---

\*Corresponding author

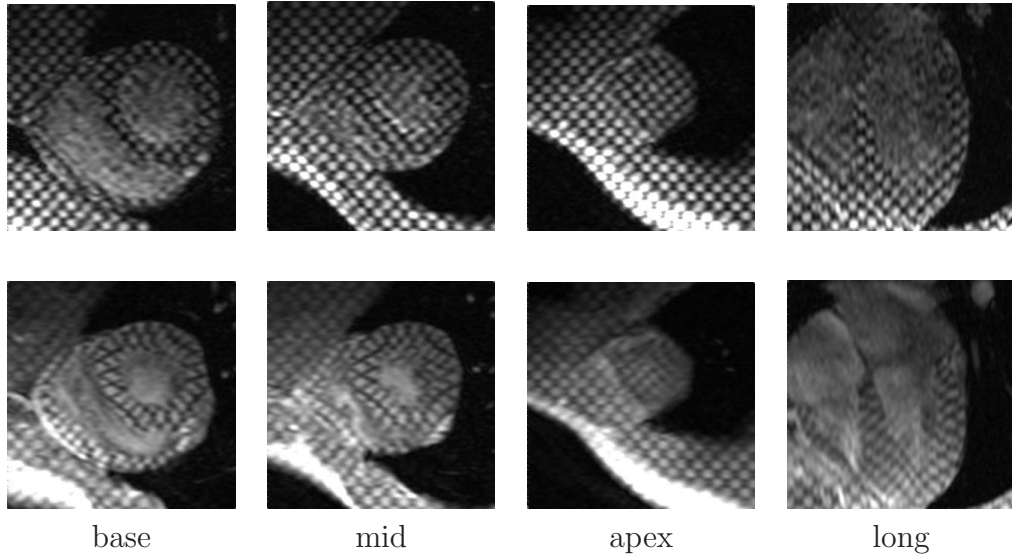


Figure 1: Example of the tMRI images of the heart. From left to right: basal, medial, apical, and longitudinal planes of the left ventricle (LV). The top row corresponds to End-of-Diastole (ED) and the bottom row to End-of-Systole (ES).

an interesting clinical application of graph-based metric estimators, showing their value for solving practical problems found in medical imaging.

## 1. Introduction

Tagged Magnetic Resonance Imaging (tMRI) is currently the reference modality for obtaining regional information on myocardial deformation. Since its introduction by Zerhouni et al. (1988) for cardiac function assessment, this technique has rapidly evolved due to advances in image acquisition, image processing, and clinical applications. Figure 1 shows an example of images of the heart obtained with tMRI. The continuous efforts of researchers to obtain a completely automatic and reliable method for recovering cardiac motion and deformation, have generated interest in this modality. Pai and Axel (2006) have presented a review of technical and clinical advances in this arena.

The estimation of cardiac displacement fields from tMRI sequences can be formulated as an image registration problem (Chandrashekhara et al., 2004a;

14 Ledesma-Carbayo et al., 2005; Petitjean et al., 2003; Radeva et al., 1997;  
 15 Shen et al., 2005), since it requires finding a point correspondence between  
 16 component frames of the sequence. The application of registration techniques  
 17 based on information theory (IT) (Chandrashekhara et al., 2004a; Petitjean  
 18 et al., 2003) is an interesting approach to cope with the non linear changes  
 19 in tag intensity along the cardiac cycle. However, the evolution of trans-  
 20 formation models towards the use of 3D + t models (Chandrashekhara et al.,  
 21 2004b; Ledesma-Carbayo et al., 2005) needs the definition of a metric of joint  
 22 alignment to optimize simultaneously the transformation parameters. This  
 23 problem can be circumvented by using a linear combination of the pairwise  
 24 metrics between each phase and the reference (Chandrashekhara et al., 2004b;  
 25 Ledesma-Carbayo et al., 2005), but this approach still measures the image  
 26 similarity with respect to the first phase and fails to exploit the temporal  
 27 correlation between phases.

28 In this paper, we have explored an extension of IT-based registration tech-  
 29 niques that finds the optimal transformation parameters of a 3D+t model by  
 30 maximization of a metric of joint frame alignment. The main challenge in  
 31 computing such metrics is the estimation of the probability density function  
 32 (PDF) from a set of samples in a high-dimensional space (in our case, the  
 33 sequence length). Neemuchwala et al. (2007) have recently presented estima-  
 34 tors of  $\alpha$ -Mutual Information  $MI_\alpha$  based on  $k$ NNG when high dimensional  
 35 features are employed, and the use of histograms is not possible due to the  
 36 curse of dimensionality (Bellman, 2003). Ma et al. (2007) have applied these  
 37 estimators for computing deformations in a synthetic sequence of tumor im-  
 38 ages, and introduced joint similarity extensions of  $MI_\alpha$ . More recently, Leo-  
 39 nenko et al. (2008) have presented a class of estimators of  $H_\alpha$  based on the  
 40  $k^{th}$  nearest-neighbor distances computed from a sample of  $N$  i.i.d. vectors  
 41 with distribution  $f$ . In this article, we have extended  $k$ NNG estimators of  
 42  $H_\alpha$  to quantify the joint alignment of multiview sequences, and applied it to  
 43 tMRI sequences to recover cardiac displacement fields. For quantitative eval-  
 44 uation of our method, a comparison was run against the method proposed by  
 45 Chandrashekhara et al. (2004a) for 6 healthy subjects. Results show a signifi-  
 46 cant decrease in positional error with respect to manually placed landmarks.  
 47 The estimated strains were compared with those obtained by cine harmonic  
 48 phase (HARP) magnetic resonance imaging as the ground truth. For as-  
 49 sessing consistency with other modalities, we have studied two patients with  
 50 myocardial infarction and compared the strain maps with the information  
 51 provided by delayed-enhancement MRI of Gadolinium (deMRI) and cardiac

52 catheterization.

## 53 2. Method

### 54 2.1. Dataset

55 The database used for the experiments consisted of 6 healthy subjects  
56 (3 females and 3 males between 24 and 33 years old) and 2 patients (males,  
57 54 and 70 years old) with transmural infarction of the myocardium. For  
58 all subjects, cine MRI (cMRI), tMRI, and deMRI images were acquired in  
59 breath-hold by using a General Electric Signa CV/i, 1.5 T scanner (General  
60 Electric, Milwaukee, USA). Healthy subjects were also imaged with deMRI  
61 to have a proof of their clinical status. The values of acquisition parameters  
62 were: slice thickness = 8mm, in-plane resolution = 0.78mm  $\times$  0.78mm, gap  
63 between slices = 0mm, TR=7.99ms, TE=4.43ms, flip angle = 20 degrees,  
64 and FOV=40cm $\times$ 40cm. cMRI and tMRI sequences were acquired at 30  
65 phases per cardiac cycle. tMRI images with a grid pattern of 5mm (tag  
66 spacing) were acquired by applying a Spatial Modulation of Magnetization  
67 (SPAMM) sequence. An expert clinician assessed the presence of infarction  
68 from deMRI images, and classified the 17 standard segments (Cerqueira et al.,  
69 2002) according to the transmural extent of necrosis in the myocardial wall into  
70 four categories: i) 0% (healthy segment) ii) <50%, iii) 50-75% and iv) >  
71 75%. For patients with myocardial infarction, cardiac catheterization was  
72 also performed to assess coronary occlusion.

### 73 2.2. Deformation model

74 Figure 2 presents a diagram of the method of joint alignment. This figure  
75 shows that the deformation of the heart is modeled by a set of transformations  
76 defined relative to its undeformed state (ED), which simplifies the compu-  
77 tation of metric derivatives and Lagrangian strains. The use of Lagrangian  
78 strains is more common than natural strains<sup>1</sup> in most of current imaging  
79 techniques (US, MR, SPECT, angiography) (Sutherland et al., 2006).

80 Typically, a tMRI study consists of two acquisitions performed in short  
81 axis (SA) and long axis (LA), which provide complementary information  
82 about the cardiac deformation. This results in two image sequences  $I_{SA}(\mathbf{x}, t)$

---

<sup>1</sup>The natural strain  $\varepsilon_N$  is defined as the integral over time of the instantaneous strain,  
i.e.  $\varepsilon_N = \int_{t_1}^{t_2} \frac{dL}{L}$

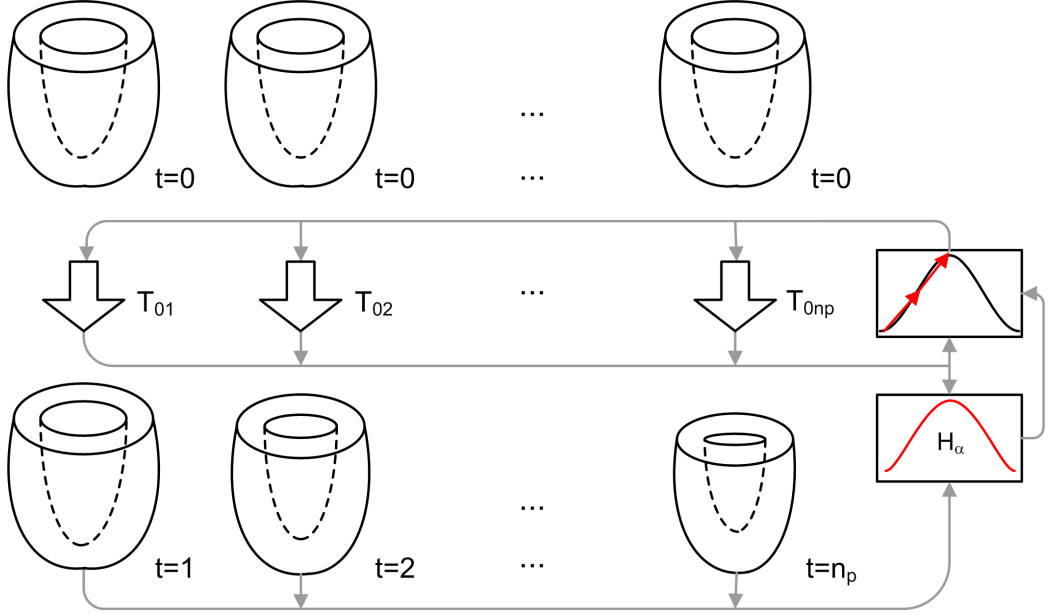


Figure 2: Cardiac motion estimation method. Transformations  $T_{0i}$  mapping points in ED (top) to phase  $i$  (bottom) are optimized simultaneously to minimize the  $H_\alpha$  of all phases. The inputs to the optimizer are the set of transformations  $\mathcal{T}$  and the metric of similarity. This metric takes in turn all images of the sequence as input.

and  $I_{LA}(\mathbf{x}, t)$  of  $P$  phases, which provide the voxel intensity at spatial position  $\mathbf{x}$  and time  $t$ . Cardiac deformation was modeled as a set of  $P - 1$  B-Splines  $\mathcal{T}(\mathbf{x}) = \{T_i(\mathbf{x})\}_{i=1:P-1}$  transformations defined on  $I_{SA}(\mathbf{x}, 0)$ . The corresponding deformations in LA can be obtained from  $\mathcal{T}(\mathbf{x})$  by composition of  $\mathcal{T}(\mathbf{x})$  with the rigid transformations defining the relationship between both coordinate systems, as described in Section 2.6.

### 2.3. Joint vs pairwise alignment

We explain the advantage of joint registration over pairwise registration by adopting a generative model representation of the image registration problem. A generative model for the image registration problem is obtained by expressing the log posterior probability of the deformation (B-spline parameters  $\mathbf{B}$ ) given the image sequence (Learned-Miller, 2006):

$$\ln p(\mathbf{B}|\mathbf{Z}) = -H(\mathbf{Z}|\mathbf{B})N + \ln p(\mathbf{B}) \quad (1)$$

where  $N$  is the total number of pixels,  $\mathbf{Z}$  is a random vector of dimension  $P$ , called a pixel stack, whose realizations are the time series of grey levels at a specified pixel location over successive image volumes in the time sequence. Each realization  $\mathbf{z}$  ranges over the set  $\{0, 2^Q\}^P$  where  $Q$  is the number of bits quantifying image intensities. In Equation 1,  $p(\mathbf{B})$  is a prior on the deformation, which can be discarded by assuming a uniform probability distribution of the transformation parameters.

The conditional entropy on the right hand side of Equation 1 can be empirically estimated from Shannon entropy using (Cover and Thomas, 1991):

$$\begin{aligned} H(\mathbf{Z}|\mathbf{B}) &= \sum_i p(\mathbf{Z}(\mathbf{x}) = \mathbf{z}_i|\mathbf{B}) \ln p(\mathbf{Z}(\mathbf{x}) = \mathbf{z}_i|\mathbf{B}) \\ &\cong -N^{-1} \sum_i N_i \ln N_i + \ln N \end{aligned} \quad (2)$$

where  $N_i = \sum_{j:\mathbf{Z}(\mathbf{x}_j)=\mathbf{z}_i}$  is the number of pixel locations where the associated vector  $\mathbf{Z}(\mathbf{x}_j)$  equals grey level  $\mathbf{z}_i$  and satisfies  $\sum_i N_i = N$ .

The problem, of course, is that there are too few samples to reliably estimate the log posterior (1) due to the curse of dimensionality. Furthermore, even if one wanted to compute the log posterior, the required memory explodes as  $P$  increases (memory scales as  $2^{P \cdot Q}$ ). This is the justification of alternative direct methods of estimating the entropy. The MST/ $k$ NNG alpha-entropy estimators converge in probability to  $H(\mathbf{Z}|\mathbf{B})$  for large  $N$  and  $P$ . This is because for large  $N$  the alpha-entropy estimator converges to the alpha-entropy, by the law of large numbers, and for large  $P$ ,  $\alpha = (P-1)/P \approx 1$ , and the alpha-entropy is approximately equal to the Shannon entropy.

Therefore, in light of the representation (1) of the log posterior density, the PA approach corresponds to making an approximation to the entropy function defining the log posterior  $H(\mathbf{Z}|\mathbf{B}) \approx \sum_{j=0}^{P-1} H(I_j, I_{j+1}|\mathbf{B})$  where  $I_j$  denotes the  $j$ -th image volume in the sequence. Such approximation to the full joint entropy is expected to be poor when a frame of the image sequence is correlated to more than just its neighboring frames, or more generally when pairwise independence of the sequence does not imply joint independence. When the decomposition of the joint distribution into pairwise successive products gives a poor approximation to the true log posterior (1), the PA method will perform poorly. For example, using standard arguments of mathematical statistics, it can be shown that in the limit as  $N$  becomes large, minimization of the pairwise entropy will give a biased estimator of

the deformation parameters  $\mathbf{B}$ , equal to the *least false estimate* of  $\mathbf{B}$  (Ripley, 1996).

#### 2.4. *kNNG entropy estimator*

Given a random vector  $\mathbf{Z} = [Z_1 \cdots Z_P]^T$  in  $\mathbb{R}^P$ , the Rényi entropy  $H_\alpha$  of order  $\alpha$  of  $\mathbf{Z}$  is defined as (Rényi, 1961):

$$H_\alpha(\mathbf{Z}) = \frac{1}{\alpha - 1} \log \int f^\alpha(Z_1, \dots, Z_P) dZ_1 \dots dZ_P \quad (3)$$

where  $f(Z_1, \dots, Z_P)$  is the PDF of  $\mathbf{Z}$ .

If  $\mathcal{Z} = \{\mathbf{z}_1, \dots, \mathbf{z}_N\}$  are the observed data (realizations of  $\mathbf{Z}$ ), a *kNNG* can be formed by all points  $\mathbf{z}_{i=1:n}$  and the edges  $\mathbf{e}_{ik} = \mathbf{z}_i - \hat{\mathbf{z}}_{ik}$  with their *k* nearest points  $\mathcal{N}(\mathbf{z}_i) = \{\hat{\mathbf{z}}_{i1}, \dots, \hat{\mathbf{z}}_{ik}\}$ . An interesting property of this type of graph is the existence of a relationship between its length and the  $H_\alpha$  of its component points:

$$\lim_{N \rightarrow \infty} \log \left( \frac{L_{\gamma,k}(\mathcal{Z})}{N^\alpha} \right)^{\frac{1}{1-\alpha}} = H_\alpha(\mathbf{Z}) + c_{kNNG} \quad (4)$$

where  $L_{\gamma,k}(\mathcal{Z})$  is the length of the graph defined as:

$$L_{\gamma,k}(\mathcal{Z}) = \sum_{\mathbf{z} \in \mathcal{Z}} \sum_{\hat{\mathbf{z}} \in \mathcal{N}(\mathbf{z})} \|\mathbf{z} - \hat{\mathbf{z}}\|^\gamma \quad (5)$$

and  $\gamma = P * (1 - \alpha)$ . In Equation 4,  $c_{kNNG} = (1 - \alpha)^{-1} \log \beta_{d,\gamma,k}$ , where  $\beta_{d,\gamma,k}$  is a known constant that depends only on  $d$ ,  $\gamma$ , and  $k$  (Yukich, 1998).

Equation 4 suggests the following estimator of  $H_\alpha(\mathbf{Z})$ :

$$\hat{H}_\alpha(\mathbf{Z}) = \frac{1}{1 - \alpha} \left( \log \frac{1}{N^\alpha} \sum_{\mathbf{z} \in \mathcal{Z}} \sum_{\hat{\mathbf{z}} \in \mathcal{N}(\mathbf{z})} \|\mathbf{z} - \hat{\mathbf{z}}\|^\gamma - \log \beta_{d,\gamma,k} \right) \quad (6)$$

The demonstration of the convergence properties of *kNNG* estimators of entropy is out of the scope of this paper, but the reader is referred to Leonenko et al. (2008), Redmond and Yukich (1996), and Hero et al. (2003) for further reading.

There is a difference between the entropy estimation approach taken by Learned-Miller (2006) and the approach adopted in this paper. Learned-Miller assumes that intensities are independently and identically distributed

149 (i.i.d.) both over all pixel locations and over all images *inside* each pixel  
150 stack. Using these two assumptions, the problem is reduced to the compu-  
151 tation of the entropy of a scalar random variable. While the assumption  
152 of independent images inside the pixel stack  $\mathbf{Z}$  is reasonable in the case of  
153 independent subjects, it can not be maintained in our case since we focus  
154 on temporal sequences where consecutive images are expected to be highly  
155 dependent. As a consequence, entropy must be estimated in a space of high  
156 dimensionality without any constraint about component independence in  $\mathbf{Z}$ .  
157 The estimator in Equation 6 only assumes i.i.d realizations of  $\mathbf{Z}$ , and there-  
158 fore is suitable for our application.

159 A drawback of the estimator given by Equation 6 is the high computa-  
160 tional cost of the graph construction, which hampers the parameter opti-  
161 mization. In the Appendix 6, we present an analytical expression for the  
162 gradient of Equation 6 reducing significantly the calculation time.

## 163 2.5. Self matches

164 Equation 6 is numerically unstable when any of the distances  $\|\mathbf{z} - \hat{\mathbf{z}}\|$  is  
165 equal to zero, i.e. in case of self matches. If  $\mathbf{Z}$  was continuous, their realiza-  
166 tions would cover the whole range of possible values, without any repetition.  
167 However, digital images are quantized and represented by a finite number of  
168 bits, and there exists the possibility of finding multiple occurrences of a spe-  
169 cific value  $\mathbf{z}^*$  in  $\mathcal{Z}$ . To circumvent this problem, Neemuchwala et al. (2007)  
170 added uniform noise to each realization, thus dispersing features inside a  
171 radius-limited neighborhood. Even when this approach effectively solves the  
172 problem, it might generate arbitrarily large values in the estimated PDF, and  
173 introduces a stochastic component in the cost function that could interfere  
174 with the optimization process.

175 In this paper, we have solved the problem of multiple occurrences by  
176 searching for nearest neighbors at a distance strictly positive, and divid-  
177 ing the distance  $\|\mathbf{z} - \hat{\mathbf{z}}\|$  by the number of occurrences  $o_{\mathcal{Z}}(\mathbf{z})$  of  $\mathbf{z}$  in  $\mathcal{Z}$ .  
178 This corrects the approximation of the probabilities by using the volume  
179 of the Voronoi cell proposed by Neemuchwala and Hero (2005) in case of  
180 self matches. Even when this requires a second nearest neighbor search, the  
181 additional computational cost is negligible (Mount, 2006).

## 182 2.6. Combination of views

183 A tMRI study typically contains SA and LA views of the heart that  
184 provide complimentary information about the cardiac deformation. An al-



ternative to include both views in the registration process is a linear combination of the similarity metrics measured independently for each view (Chandrasekara et al., 2004a). However, the application of this strategy would be in conflict with the underlying ideas of this paper, which studies a manner of quantifying the alignment of a sequence as a whole. To obtain an unique metric valid for multiple views and multiple frames, each view can be considered a source of realizations of the same random vector  $\mathbf{Z}$ . This means that pixel stacks  $\mathbf{z}^{sa}$  and  $\mathbf{z}^{la}$  taken from SA and LA are considered as realizations of the same variable  $\mathbf{Z}$ , and can thus be mixed into a single set of samples  $\mathcal{Z}$ . Under this hypothesis, Equation 3 remains unchanged for registration of multiple view sequences, integrating in this way information from different time points and views into the same unified framework.

By convention, SA has been taken as the reference space for defining the transformation. Thus, the coordinates of samples in LA must be mapped to SA to be transformed. These transformed coordinates need then to be mapped back to LA for computing the pixel stack  $\mathbf{z}^{la}$ . Therefore, it is necessary to know the transformations from SA to LA ( $T_{sl}$ ) and from LA to SA ( $T_{ls}$ ). These transformations are provided by the DICOM format in the form of image origin  $\mathbf{o}_w^{sa}$  and orientation  $\mathbf{D}_w^{sa} = [\mathbf{i}^{sa} \ \mathbf{j}^{sa} \ \mathbf{k}^{sa}]$  ( $\mathbf{o}_w^{la}$  and  $\mathbf{D}_w^{la} = [\mathbf{i}^{la} \ \mathbf{j}^{la} \ \mathbf{k}^{la}]$ ) with respect to the coordinate system of the scanner. Two generic points  $\mathbf{x}_i^{sa}$  and  $\mathbf{x}_i^{la}$  in image coordinates can be expressed in world coordinates as :

$$\mathbf{x}_w^{sa} = \mathbf{o}_w^{sa} + \mathbf{D}_w^{sa} \mathbf{x}_i^{sa} \quad (7)$$

$$\mathbf{x}_w^{la} = \mathbf{o}_w^{la} + \mathbf{D}_w^{la} \mathbf{x}_i^{la} \quad (8)$$

When Equations 7 and 8 refer to the same physical point, we can equate the right sides and obtain the following transformations between views:

$$T_{sl} : \mathbf{x}_i^{sa} \rightarrow \mathbf{x}_i^{la} = (\mathbf{D}_w^{la})^T \mathbf{D}_w^{sa} \mathbf{x}_i^{sa} + (\mathbf{D}_w^{la})^T (\mathbf{o}_w^{sa} - \mathbf{o}_w^{la}) \quad (9)$$

$$T_{ls} : \mathbf{x}_i^{la} \rightarrow \mathbf{x}_i^{sa} = (\mathbf{D}_w^{sa})^T \mathbf{D}_w^{la} \mathbf{x}_i^{la} + (\mathbf{D}_w^{sa})^T (\mathbf{o}_w^{la} - \mathbf{o}_w^{sa}) \quad (10)$$

## 2.7. Strain estimation

The mechanical impairment induced over time due to myocardial infarction is an important issue that can be assessed through tMRI (Axel et al., 2005). The infarcted region of diseased myocardium permanently loses its

214 ability to contract, and this is manifested in an altered motion during the  
 215 cardiac cycle. Therefore, there should be a correlation between the local-  
 216 ization of the infarction and corresponding local strains. To study this cor-  
 217 respondence, strain was computed from the recovered displacements fields  
 218 to discriminate between active healthy myocardium and passively moving  
 219 infarcted tissue.

220 The set of transformations  $\mathcal{T}$  allows to compute the displacement field  
 221  $\mathbf{u}(\mathbf{x}, t)$  as a function of position  $\mathbf{x}$  at ED and time  $t$ . Since the assumption of  
 222 small deformations is too strong for cardiac deformations, the Green strain  
 223 tensor cannot be applied, and the Green-Lagrange strain tensor must be used  
 224 instead. The Green-Lagrange strain tensor is defined as (Belytschko et al.,  
 225 2001)

$$\mathbf{E} = \frac{1}{2} (\nabla \mathbf{u} + \nabla \mathbf{u}^T + \nabla \mathbf{u}^T \nabla \mathbf{u}) \quad (11)$$

226 Diagonal elements  $E_{ii}$  of  $\mathbf{E}$  are normal strains, i.e. strains along each direction  
 227 in the rectangular coordinate system. Given the geometry of the heart, it is  
 228 preferable to use a local coordinate system composed by radial, circumferen-  
 229 tial, and longitudinal directions (Figure 3). To estimate the epicardial surface  
 230 necessary to obtain the radial direction, a manual segmentation of the SA im-  
 231 age at ED was performed followed by the application of a variant (Schroeder  
 232 et al., 1998) of the original marching cubes algorithm (Lorensen and Cline,  
 233 1987).

234 The normal strain along an arbitrary direction  $\mathbf{d}$  can be obtained from  
 235 Equation 11 as (Petitjean et al., 2005):

$$E_{dd} = \mathbf{d}^T \mathbf{E} \mathbf{d} \quad (12)$$

236 Radial ( $E_{rr}$ ), circumferential ( $E_{cc}$ ), and longitudinal ( $E_{ll}$ ) normal strains can  
 237 be obtained by replacing  $\mathbf{d}$  with directions  $\mathbf{r}$ ,  $\mathbf{c}$ , and  $\mathbf{l}$ , respectively.

238 The radial direction is defined outward and perpendicular to the epicar-  
 239 dial surface. The circumferential direction is in the short-axis plane (perpen-  
 240 dicular to the long axis), parallel to the epicardial surface, and counterclock  
 241 wise, as viewed from the base. The longitudinal direction is obtained as the  
 242 cross product of radial and circumferential directions, tangent to the epicar-  
 243 dial surface. In this way, directions were defined to create a right-handed  
 244 system.

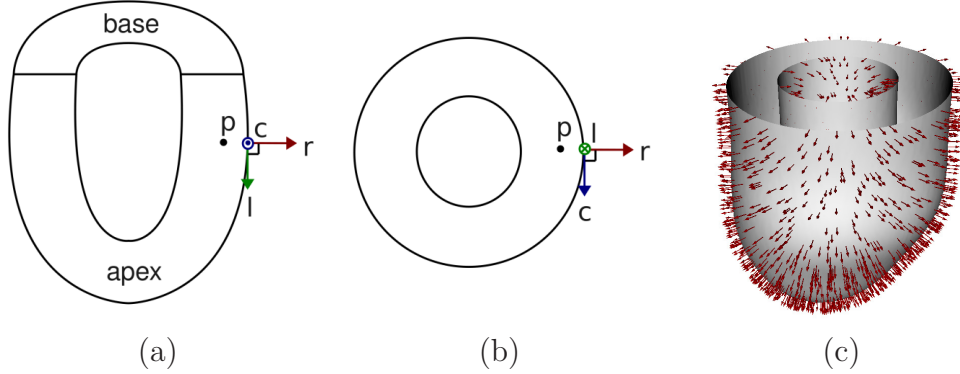


Figure 3: Local coordinate system used for strain analysis. Radial ( $\mathbf{r}$ ), circumferential ( $\mathbf{c}$ ), and longitudinal ( $\mathbf{l}$ ) directions for the point  $\mathbf{p}$  are shown in the longitudinal (a) and transverse (b) views of the LV. (c) Example of radial directions obtained from the epicardial and endocardial surfaces of the LV.

## 2.8. Implementation issues

A registration-based method is composed by a transform, a metric, an interpolator, and an optimizer. In the following we describe the parameters used for each of these components in this paper. Unless the contrary is specified, the implementation of the method was performed by using the Insight Toolkit (Ibanez et al., 2008), and its component classes.

For the transformation (Section 2.2), the only parameters to specify are the spacings between control points in  $x$ ,  $y$ , and  $z$  directions. We have set these spacings equal to the tag spacing (5-7mm for our dataset). A larger spacing could be insufficient to describe the deformations provided for all tags (for example, if the spacing was twice the tag spacing there would be two control points to fit three tags). On the other hand, finer grids add unnecessary degrees of freedom to the transform (there are not material points to track between two adjacent tags) and make the optimization process more difficult. This was confirmed experimentally.

Regarding the metric (Equation 6), the value of  $\alpha$  was set to 0.9, which implies a  $\gamma$  value of 1.0 when considering 10 frames as the length of systole. The number  $N$  of points  $\mathbf{z}$  (i.e.  $\#\mathcal{Z}$ ) was set to  $0.2 \times N_{max}$ ,  $N_{max}$  being the number of points in the region of interest. The construction of the kd-tree and the nearest neighbor search was performed by using the approximate nearest neighbors (ANN) library (Mount, 2006). The use of low  $k$ -values (for

example  $k = 1$ ) led to misregistration of the sequences used in this paper, probably a consequence of a noisy estimation of the entropy. The use of several neighbors makes the entropy estimator more robust to noise, since the addition of the distances to the considered point in Equation 6 tends to cancel the noise in the measurements. A number  $k = 20$  of nearest neighbors yielded satisfying results.

For interpolation, we have used a linear interpolator. For optimization, we have used a gradient descent method with learning rate  $\eta = 1mm$  and a maximum number of iterations  $N_{it} = 200$ . The range of variation of the transformation parameters typically increases from end-systole to end-diastole, which creates optimization problems when starting from an identity transform. This type of problem may be solved by setting different scales to the parameters according to a priori information about the specific problem (Ibanez et al., 2008), but this solution led to a sequence misregistration. Therefore we reduced the range of variation of the parameters for all frames by initializing the optimizer with the result of a pairwise registration of each frame with respect to the first one ( $P = 2$ ). This solution allowed us to obtain good results after joint registration, and it does not assume any priors on the deformation.

### 3. Results

#### 3.1. Entropy evolution

As the  $H_\alpha$  is minimized during the registration process, the distribution of the pixel stack  $\mathcal{Z}$  after registration should be more compact with respect to the original data. To visualize this expected change in distribution, we have performed a reduction of dimensionality by applying a Principal Components Analysis (PCA) (Rao, 2002) and projected  $\mathcal{Z}$  in the subspace spanned by the first three principal directions  $\mathbf{q}_{i=1:3}$ . Figure 4 shows that the point distribution before registration presents a larger variance than after registration, equivalent to a state of higher entropy, as expected.

#### 3.2. Error analysis

Figure 5 presents an example of the deformation fields obtained by joint image registration, showing consistency with cardiac physiology. To compute accuracy, tag intersections were marked in the systolic phases of 6 healthy subjects by an expert clinician. Only systolic phases were marked since the

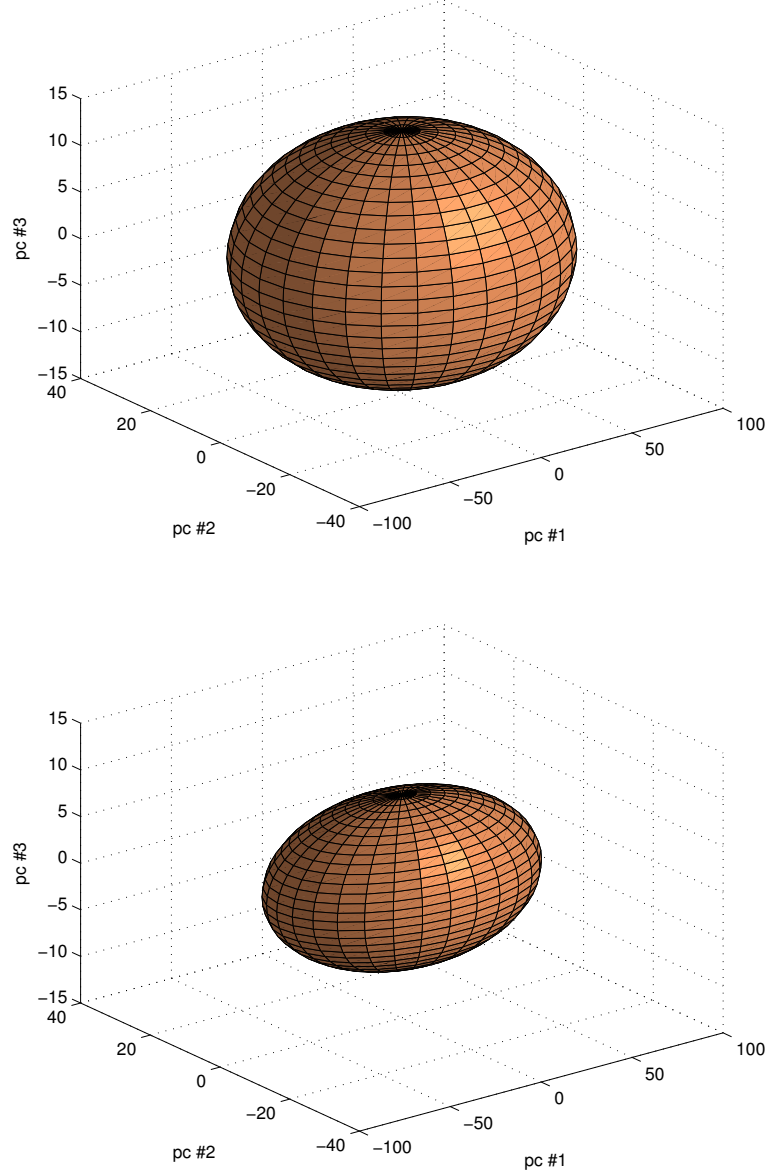


Figure 4: Distributions of the pixel stack  $\mathbf{Z}$  in the subspace spanned by the first three principal component directions  $\mathbf{q}_{i=1:3}$ . Top: before registration; bottom: after registration. Ellipsoids have semi-axis lengths equal to the standard deviation along the corresponding principal vectors  $\mathbf{q}$ .

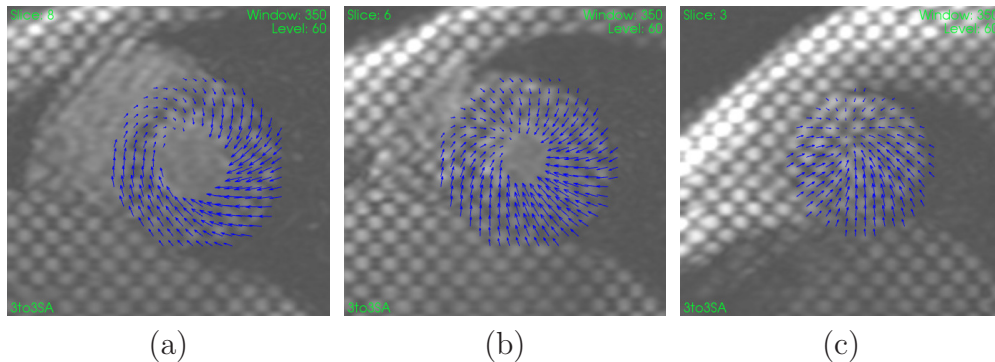


Figure 5: Example of displacement field at ES (relative to ED) for a healthy volunteer at (a) base, (b) mid, and (c) apex. The displacement field is plotted on the SA images at ED.

Table 1:  $p$ -values obtained from the Mann-Whitney test performed on the MSE errors for JA and PA methods. Results are provided for equally spaced time instants along systole. Bold values mean rejection of the null hypothesis at 5% significance level.

<i>time</i> (relative to systole)	14%	28%	43%	57%	71%	86%	100%
<i>p</i> -value	< <b>0.01</b>	<b>0.01</b>	< <b>0.01</b>	<b>0.01</b>	0.01	<b>0.01</b>	< <b>0.01</b>

images were acquired by using SPAMM, and the strong fading effect of this sequence makes difficult to identify tags beyond ES. The resulting transformations  $\mathcal{T}^*$  were used to propagate the points in ED to the remaining phases, and compare to manual measurements. Tag intersections were marked in SA at base, mid, and apex, whereas only the central plane was used in LA. On average, 24 tag intersections were tracked from ED through systole.

To study the differences with respect to pairwise methods, we have implemented the method proposed by Chandrashekar et al. (2004a) by using the Insight Toolkit (Ibanez et al., 2008), and compared the Mean Square Errors (MSE) along systole (Figure 6). A lower MSE was obtained for almost all cardiac phases, and a Mann-Whitney test (Altman, 1997) was performed to assess the statistical significances of these differences. The normality of the distribution was verified at level 0.05 by using a Lilliefors test (Lilliefors, 1967), and the independence of population ensured by applying each method to a different set of three sequences. Table 1 shows rejection of the null hypothesis at 5% significance level for almost all phases, meaning that the differences in MSE are statistically significant.

Differences in error variance (Figure 7) were also studied to assess the

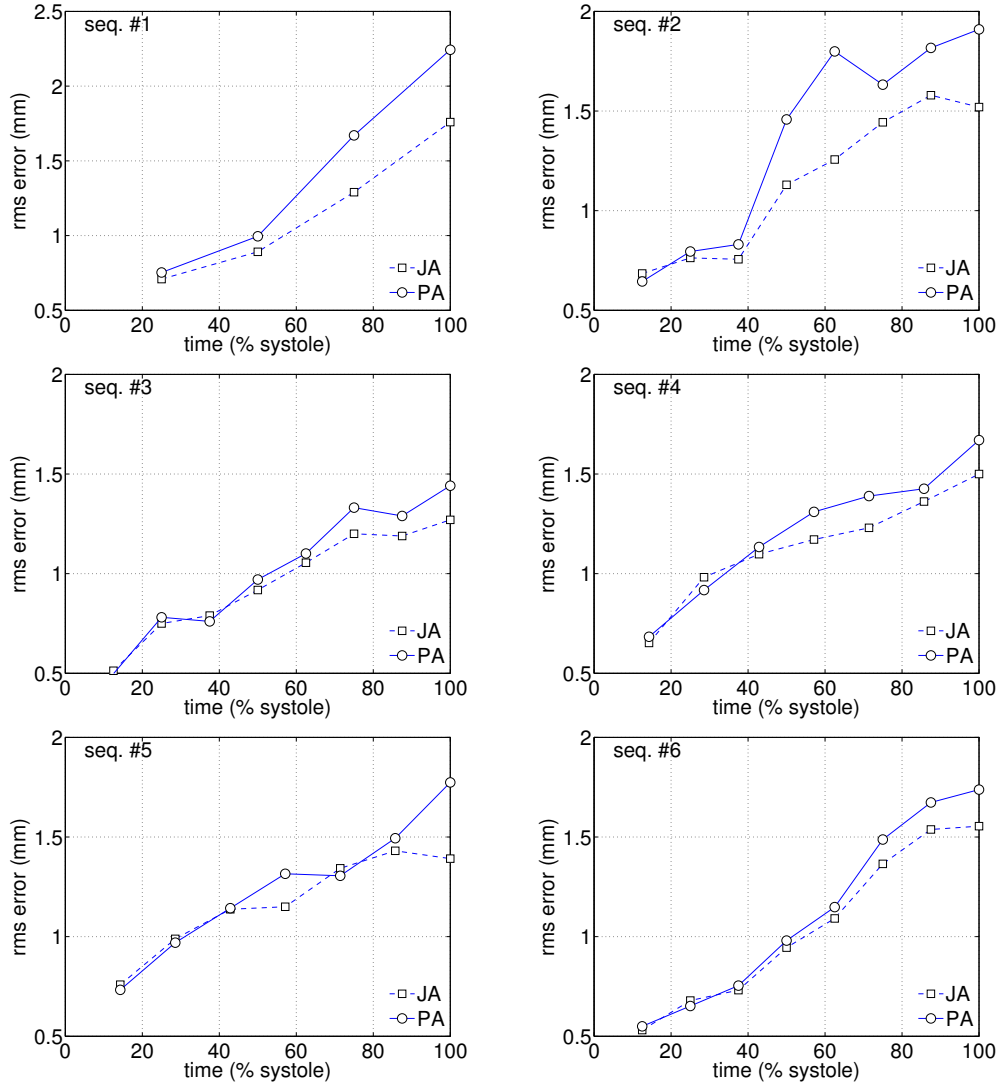


Figure 6: MSE errors between manually placed landmarks at tag intersections, and propagated landmarks for six healthy volunteers. JA = joint alignment; PA = pairwise alignment.

Table 2:  $p$ -values obtained with a F-test performed on error variances for JA and PA methods. Bold values mean rejection of the null hypothesis of equal variances ( $p=0.05$ ).

$t$ (relative to systole)	14%	28%	43%	57%	71%	86%	100%
$p$ -value	0.29	<b>0.04</b>	<b>&lt; 0.01</b>	<b>&lt; 0.01</b>	<b>&lt; 0.01</b>	<b>0.04</b>	<b>0.01</b>

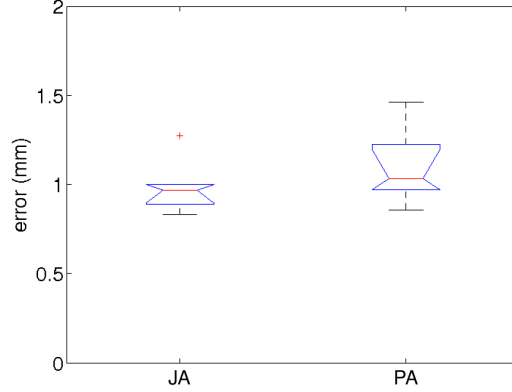


Figure 7: Box plots of the MSE errors showing the difference in variance between joint alignment (JA) and pairwise alignment (PA).

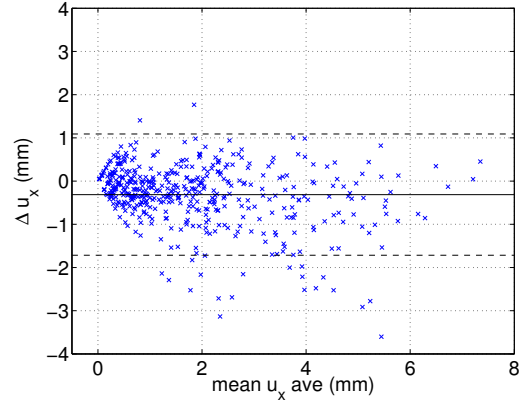
uniformity of the registration error across regions. It is desirable that registration accuracy be independent of the displacement magnitude, which varies across the myocardium during the cardiac cycle. The error uniformity can be measured by computing its variance. Table 2 shows the  $p$ -values obtained from a F-test (Altman, 1997) performed on the variances for each phase. As in the previous Mann-Whitney test for mean error values, each method was applied on different sequences to ensure independence.

Finally, the JA method was compared to manual measurements by using Bland-Altman plots (Altman, 1997). Figure 8 shows a negligible bias, and a symmetric error distribution around it.

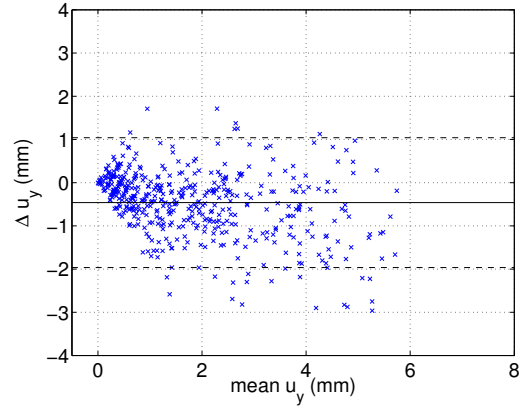
### 3.3. Computational complexity and speed

Registration based on graphs suffers from a high computational cost that increases with the number of feature realizations. The reduction in complexity by analytical computation of the gradient of the cost function is especially advantageous when using transformations with high number of parameters. For example, if B-Splines are employed, even a coarse grid over the LV of  $8 \times 8 \times 8$  control points contains 1,536 parameters, and the gradient estimation requires 3,072 function evaluations, i.e. building 3,072 graphs. The use of

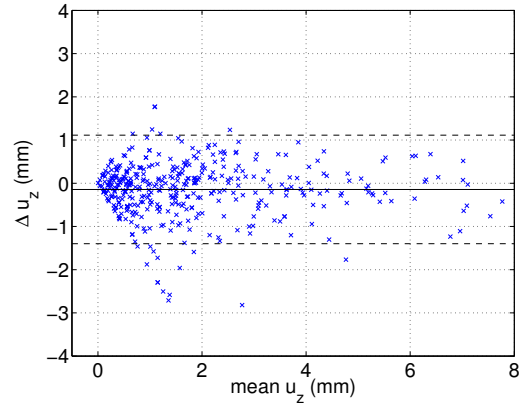




(a)



(b)



(c)

Figure 8: Bland-Altman plots of displacements along  $x$  (a),  $y$  (b), and  $z$  (c) axes ( $\Delta u_x, \Delta u_y$ , and  $\Delta u_z$ ). Solid and dashed lines show respectively the mean value and the 95% confidence interval of point displacements.

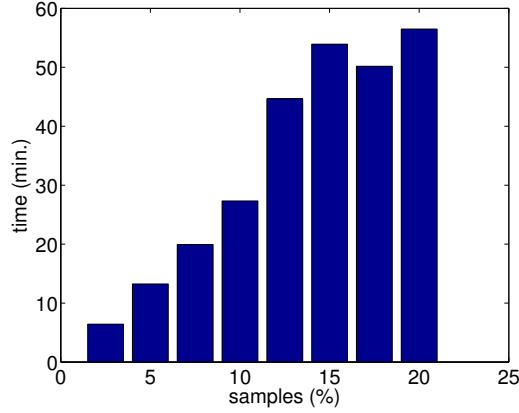


Figure 9: Average registration time as a function of the number of samples used for estimating  $H_\alpha$  (expressed as percent of the number of voxels of the ROI containing the LV)

analytical expressions resulted in an average computation time of 45 min for a PC with a 64 bits processor Intel Itanium at 1.5 GHz running Linux Suse 9.2. Figure 9 shows a linear increase in computation time with the number of points used to estimate  $H_\alpha$  (the size of  $\mathcal{Z}$ ).

#### 3.4. Strain in healthy subjects

Strain analysis along systole was performed by dividing the LV into the standard 16 segments of the American Heart Association (AHA) (Cerqueira et al., 2002) (the 17<sup>th</sup>, apical segment is optional). The average and standard deviation of radial, circumferential, and longitudinal strain were computed for the 6 healthy subjects. The strain analysis was constrained to systole because of the same data acquisition issues mentioned in Section 3.2. Figure 10 shows the mean strain along systole for healthy subjects. Radial strain presented the highest variability in agreement with previous reports (Moore et al., 2000; Petitjean et al., 2004). The strain sign is consistent with the heart physiology: during systole there is a radial thickening (positive strain), and circumferential and longitudinal shortening (negative strain).

Our method was compared to cine harmonic phase (HARP) magnetic resonance imaging method (Osman et al., 1999) as the ground truth (Figure 11). The datasets were analyzed at the Johns Hopkins University using

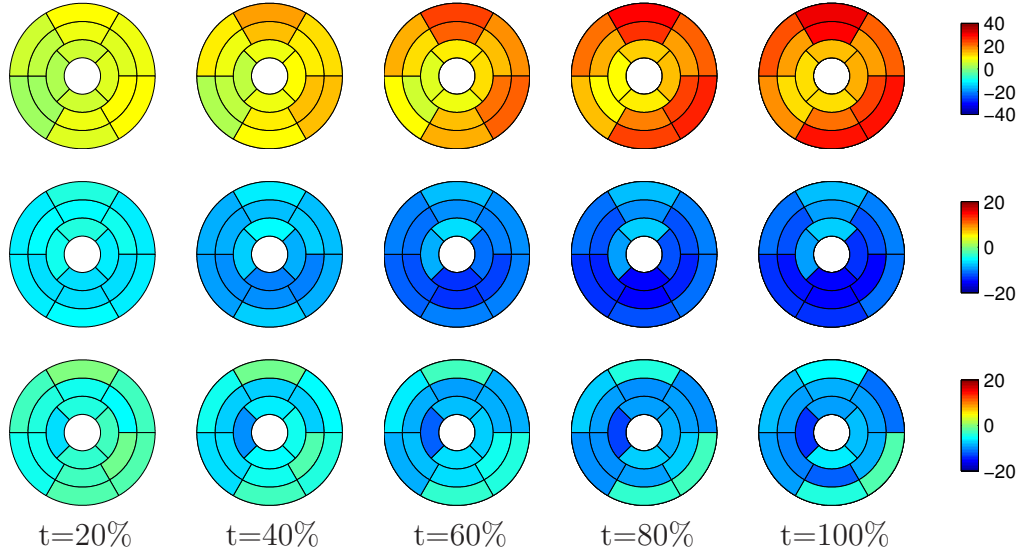


Figure 10: Mean strain over systole for healthy subjects estimated with our method. Top row: radial strain; middle row: circumferential strain; bottom row: longitudinal. Time is expressed as percent of systole.

356 Diagnosoft<sup>2</sup>, a state-of-the-art software for cardiac image analysis.

### 357 3.5. Strain in myocardial infarction

358 To assess consistency of the results with expected deformations in patho-  
 359 logical cases, a strain analysis was performed on two patients with myocardial  
 360 infarction. Figure 12 shows the infarction location, regions at risk, and cir-  
 361 cumferential strains for these patients. This analysis consisted in a segment-  
 362 to-segment comparison of circumferential strain with respect to the normal  
 363 subjects. The choice of circumferential strain for comparison is due to the  
 364 small intersubject variability of healthy subjects as compared to radial and  
 365 longitudinal strain. This makes easier the detection of any deviation in strain  
 366 with respect to normal values. Figure 12 shows that for patient #1 the largest  
 367 deviations with respect to normality are found in segments BI, MI, and AI,  
 368 coinciding with the infarction location at the inferior area of the LV. Seg-  
 369 ments BA, MA, and BAS showed an increased strain on the opposite side

---

<sup>2</sup><http://www.diagnosoft.com>

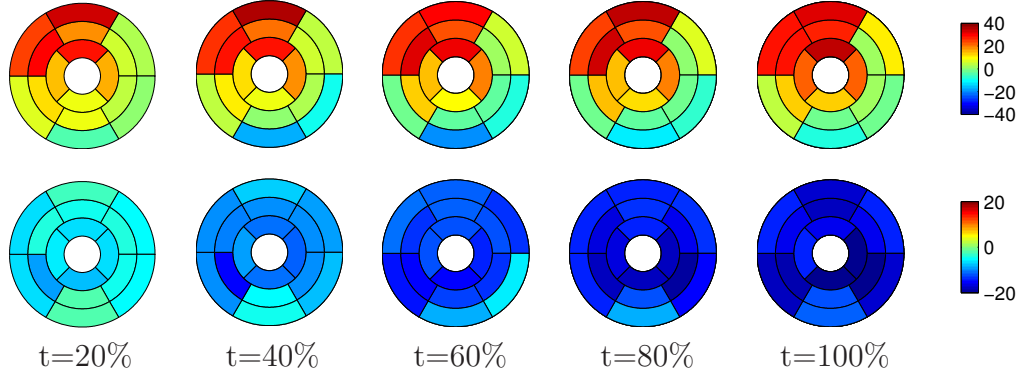


Figure 11: Mean strain over systole for healthy subjects estimated by using HARP. Top row: radial strain; bottom row: circumferential strain. Time is expressed as percent of systole. Longitudinal strains are not included because Diagnosoft processes short-axis images only.

of the infarction, which could be explained as a compensatory mechanism of healthy segments to maintain the systolic function close to normal level. In patient #2, all infarcted segments presented a lower strain with respect to the control group. Even when the lateral wall had no evidence of infarction according to deMRI, the circumflex artery (the artery feeding this region) presented a 75% of occlusion, which could explain the low strains obtained for this region.

#### 4. Discussion

The MSE with respect to manual measurements obtained by JA was shown to be significantly lower than for the PA approach. The  $p$ -values obtained from the Mann-Whitney test (Table 1) show significant differences at 5% level between the errors obtained with PA and JA for most of the analyzed time points. The simultaneous parameter optimization guided by a joint metric suggested a uniform error distribution over time, but Figure 6 shows an increase in the MSE over time. To find an explanation to these results, manual measurements were repeated for two sequences to measure the intraobserver error over time. Figure 13, shows an increase in this error, meaning that intersections are more difficult to define for phases close to ES. This could be a consequence of the out-of-plane motion (tag intersections disappear from a slice), and the presence of artifacts produced by

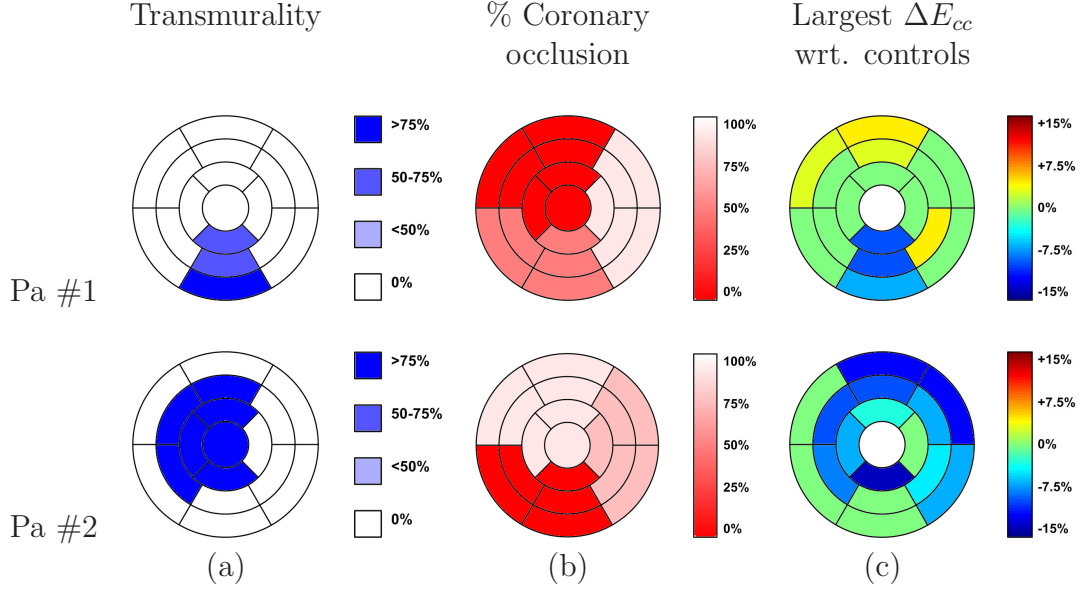


Figure 12: Relationship between infarction location, coronary occlusion *at risk*, and circumferential strains for the patients with MIA. (a) Transmurality of necrosis classified into four categories: i) 0% (healthy segment) ii) <50%, iii) 50-75% and iv) > 75%. (b) Percent of occlusion of the corresponding coronary artery. (c) Highest difference in circumferential strain with respect to the mean of the control group along systole. Differences lower than the standard deviations were arbitrarily set to zero.

off-resonance and velocity-induced phase discontinuities (Kim et al., 2003) (Figure 14). Therefore, there are some points in the myocardium for which a correspondence cannot be found for all time points, which hampers an accurate recovery of deformation. The availability of real 3D acquisitions (Rutz et al., 2008) could contribute to flatten out the error over time, since out-of-plane motion would not affect the tag pattern in this case.

The initial pairwise registration of our method only provides a coarse initialization aiming to set the parameters inside the region of capture of the joint metric. After this initialization, the mean error is approximately 25% higher than the error provided by the method by Chandrashekara et al. (2004a) ( $1.32 \pm 0.12mm.$  and  $1.06 \pm 0.12mm.$  respectively). After joint registration the error is 10% lower with respect to the same method of reference ( $0.95 \pm 0.05mm.$ ).

In this paper, the strain analysis was constrained to systole only because

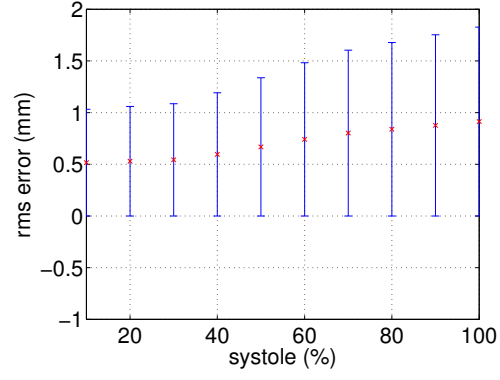


Figure 13: Intraobserver MSE error of manually placed landmarks at tag intersections.

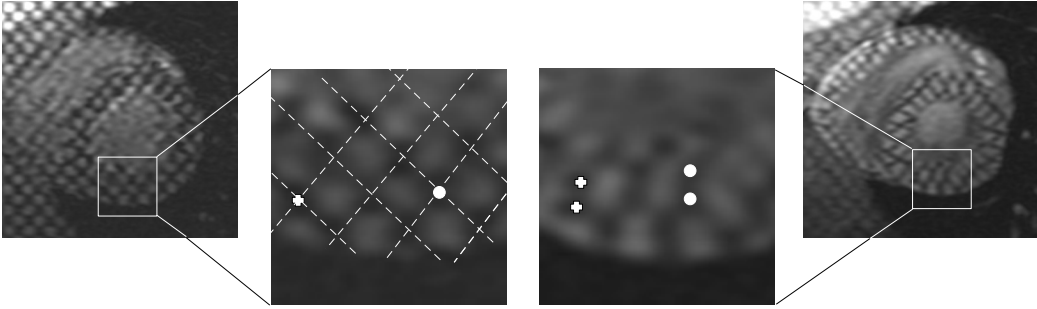


Figure 14: Tag distortion and its influence on the intraobserver error. A magnification of tags shows an ambiguity in point correspondence between ED (left) and ES (right) images. For the cross and circle at ED, there are two possible corresponding points at ES.

the tag fading precludes an accurate strain estimation beyond ES. Tag fading is quite strong in images acquired using SPAMM, and other sequences like CSPAMM have been developed to reduce this problem (Fischer et al., 1993). *A priori*, there are no apparent problems preventing the application of the presented method to the whole cardiac cycle. Similar data acquisition issues explain the exclusion of the right ventricle (RV) of the analysis. The minimum tag spacing provided by the scanner used in this paper was not sufficient to calculate strains accurately in the RV, but it could be included in the analysis in case of suitable image resolution is available.

There is an underestimation of the strain values reported in this paper. The first frame of the sequence is usually discarded since the blood is still magnetized in ED, and because of the presence of artifacts similar to those produced by off-resonance and velocity-induced phase discontinuities (Kim et al., 2003). As a consequence, the estimated strain values are lower than the real ones, and this could partially explain the differences found with the reported values in the literature. In our data, there are 10 frames during systole (in average), and therefore the discarded frames represent a loss of 10% approximately.

The strain values reported in the literature are very variable, which makes difficult a direct comparison to our results. This variability is a consequence of differences in the datasets and the estimation methods. An issue frequently disregarded is the presence of respiration artifacts and their implications on cardiac segmentation. Even when in this paper sequences presenting severe artifacts of this type were discarded, this problem is still present to some degree in all sequences, producing random local changes in the surface curvature (and therefore in the radial direction). On the contrary, circumferential direction is always in the plane of image acquisition, and does not change among subjects, which could explain the low variability of strain in this direction. Some methods to remove respiration artifacts in cMRI have been proposed (Chandler et al., 2006; Lötjönen et al., 2004), but they need to be modified for tMRI images. A possibility is to apply tag removal methods (Quian et al., 2007), before using the previously mentioned techniques.

Figures 10 and 11 show that HARP provides similar results with respect to the circumferential strain. However, the radial strain estimated by HARP shows some inhomogeneities over the left ventricle, with negative values in the inferior and inferolateral regions. In comparison, the presented method provided a more homogeneous distribution of the radial strain over systole, which is more consistent with the current knowledge of the cardiac physiology.

Note that the range of variation of the strain values is similar for HARP and our method (the color scales used in Figures 10 and 11 are exactly the same). The inclusion of the LA view is one of the sources of the differences obtained with respect to HARP, but it’s not the only one because our method incorporates temporal information as well. Based on the experiments we have performed, we are unable to attribute the differences to a single source. We have compared both methods as a whole and a further analysis should be performed to fully answer this question.

Preliminary tests on patients with myocardial infarction showed an agreement between the recovered and expected strain. Full correspondence between infarcted regions and low strain values was found, in agreement with previous results from studies with 2D US (Becker et al., 2006; Chan et al., 2006; Jurcut et al., 2008; Sachdev et al., 2006; Vartdal et al., 2007; Zhang et al., 2005) and MRI (Garot et al., 2004; Geskin et al., 1998; Korosoglou et al., 2008; Spottiswoode et al., 2007). These experiments are only illustrative, and show consistent strains values compared to other modalities.

## 5. Conclusions

In this paper, we have used JA of tMRI sequences for cardiac motion estimation, motivated by the promising results reported for methods based on information-theoretic metrics, and from a probabilistic point of view in Section 2.3. To cope with the high computational cost of the  $k$ NNG estimators of  $H_\alpha$ , an analytical expression for metric derivatives was obtained, resulting in a  $O(N \log N)$  complexity, which reduces drastically the registration time. The strategy to combine different views performed correctly, resulting in a simple way of integrating their information into a unified metric that measures multiphase and multiview similarity in image sequences. Results showed significantly lower mean errors and variances when compared to a standard PA approach. Strain values corresponding to healthy subjects were similar to those reported in the literature. However, the lack of standardization, and the high number of sources of variability, make a direct comparison difficult. Strain values for patients with myocardial infarction showed an excellent visual correlation with infarction location and territories at risk. Even when these results are encouraging, experiments need to be extended to a larger population to confirm and generalize clinical conclusions. In this paper, we have shown an interesting clinical application of graph-based metric estimators, showing their value for solving practical problems found in



478 medical imaging.

## 479 6. Appendix: analytical derivatives

480 Many optimizers need to estimate the gradient of the cost function. To  
 481 this purpose, the use of finite difference approximation to the gradient is  
 482 impractical for transformations with high number of parameters, since it  
 483 requires computing a  $kd$ -tree for each perturbation of the set of parame-  
 484 ters. This is especially problematic for high-dimensional feature spaces as  
 485 the number of perturbations requires for the finite difference estimator is  $D$ .  
 486 This problem of graph-based estimators has been addressed by Sabuncu and  
 487 Ramadge (2005) for Minimum Spanning Tree (MST) estimators of  $H_\alpha$ . Here  
 488 we develop a similar analytical approximation.

489 Using Equation 6, the derivative with respect to the parameter  $m$  of the  
 490 transformation is

$$\begin{aligned}
 \frac{\partial}{\partial p_m} \hat{H}_\alpha &= \frac{\frac{\partial}{\partial p_m} \left( \sum_{\mathbf{z} \in \mathcal{Z}} \sum_{\hat{\mathbf{z}} \in \mathcal{N}(\mathbf{z})} \|\mathbf{z} - \hat{\mathbf{z}}\|^\gamma \right)}{(1 - \alpha) \sum_{\mathbf{z} \in \mathcal{Z}} \sum_{\hat{\mathbf{z}} \in \mathcal{N}(\mathbf{z})} \|\mathbf{z} - \hat{\mathbf{z}}\|^\gamma} \\
 &= \frac{\sum_{\mathbf{z} \in \mathcal{Z}} \sum_{\hat{\mathbf{z}} \in \mathcal{N}(\mathbf{z})} \frac{\partial}{\partial p_m} (\|\mathbf{z} - \hat{\mathbf{z}}\|^2)^{\frac{\gamma}{2}}}{(1 - \alpha) \sum_{\mathbf{z} \in \mathcal{Z}} \sum_{\hat{\mathbf{z}} \in \mathcal{N}(\mathbf{z})} \|\mathbf{z} - \hat{\mathbf{z}}\|^\gamma} \\
 &= \frac{P \sum_{\mathbf{z} \in \mathcal{Z}} \sum_{\hat{\mathbf{z}} \in \mathcal{N}(\mathbf{z})} \|\mathbf{z} - \hat{\mathbf{z}}\|^{\gamma-2} \frac{\partial}{\partial p_m} (\|\mathbf{z} - \hat{\mathbf{z}}\|^2)}{2 \sum_{\mathbf{z} \in \mathcal{Z}} \sum_{\hat{\mathbf{z}} \in \mathcal{N}(\mathbf{z})} \|\mathbf{z} - \hat{\mathbf{z}}\|^\gamma}
 \end{aligned} \tag{13}$$

491 The problem has been reduced to computation of derivatives  $\|\mathbf{z} - \hat{\mathbf{z}}\|^2$ .  
 492 By assuming no changes in correspondence between a point  $\mathbf{z}$  and its nearest  
 493 neighbor  $\hat{\mathbf{z}}$  for infinitesimal changes in the transformation parameters, these  
 494 derivatives can be computed as:

$$\frac{\partial}{\partial p_m} (\|\mathbf{z} - \hat{\mathbf{z}}\|^2) = \sum_{j=1}^P 2(z_j - \hat{z}_j) (\mathbf{J}_T^m(\mathbf{x}_j))^T \nabla z_j \tag{14}$$

495 where  $\nabla z_j$  is the intensity gradient at the point  $\mathbf{x}_j = T_j(\mathbf{x})$ , and  $\mathbf{J}_T^m$  is the  
 496  $m^{th}$  column of the parametric jacobian of the transformation (Ibanez et al.,  
 497 2008):

$$\mathbf{J}_T = \begin{bmatrix} \frac{\partial x_1}{\partial p_1} & \frac{\partial x_1}{\partial p_2} & \dots & \frac{\partial x_1}{\partial p_m} \\ \frac{\partial x_2}{\partial p_1} & \frac{\partial x_2}{\partial p_2} & \dots & \frac{\partial x_2}{\partial p_m} \\ \vdots & \vdots & \ddots & \vdots \\ \frac{\partial x_n}{\partial p_1} & \frac{\partial x_n}{\partial p_2} & \dots & \frac{\partial x_n}{\partial p_m} \end{bmatrix}. \tag{15}$$

498 Finally, by including Equations 14 into Equation 13, the following expres-  
 499 sion is obtained for the derivative of the  $H_\alpha$ :

$$\frac{\partial}{\partial \mathbf{p}} \hat{H}_\alpha = \frac{P \sum_{\mathbf{z} \in \mathcal{Z}} \sum_{\hat{\mathbf{z}} \in \mathcal{N}(\mathbf{z})} \|\mathbf{z} - \hat{\mathbf{z}}\|^{\gamma-2} \sum_{j=1}^P 2(z_j - \hat{z}_j)(\mathbf{J}_T(\mathbf{x}_j))^T \nabla z_j}{2 \sum_{\mathbf{z} \in \mathcal{Z}} \sum_{\hat{\mathbf{z}} \in \mathcal{N}(\mathbf{z})} \|\mathbf{z} - \hat{\mathbf{z}}\|^\gamma} \quad (16)$$

500 It is important to highlight at this point, that Equation 13 is a completely  
 501 general expression and can be used for any type of matching features. If  $\mathbf{z}_i$   
 502 are concatenations of features in  $\mathbb{R}^d$  for each time point  $j$ , Equation 14 turns  
 503 into

$$\frac{\partial}{\partial p_m} (\|\mathbf{z} - \hat{\mathbf{z}}\|^2) = \sum_{j=1}^P \sum_{k=1}^d 2(z_{jk} - \hat{z}_{jk})(\mathbf{J}_T^m(\mathbf{x}_j))^T \nabla z_{jk} \quad (17)$$

504 where  $\nabla z_{jk}$  represents the spatial gradient of the  $k^{th}$  feature coefficient at  
 505 time  $j$ , and its computation depends on the feature definition.

506 By applying Equation 16 for computing derivatives, the time complexity  
 507 is reduced to  $O(N \log N)$  as compared to the  $O(N^2 \log N)$  time complexity  
 508 required for finite differences.

## 509 References

- 510 Altman, D., 1997. Practical Statistics for Medical Research. Chapman &  
 511 Hall.
- 512 Axel, L., Montillo, A., Kim, D., August 2005. Tagged magnetic resonance  
 513 imaging of the heart: A survey. Med Image Anal 9 (4), 376–93.
- 514 Becker, M., Bilke, E., Kühl, H., Katoh, M., Kramann, R., Franke, A., Bücker,  
 515 A., Hanrath, P., R., H., August 2006. Analysis of myocardial deformation  
 516 based on pixel tracking in two dimensional echocardiographic images en-  
 517 ables quantitative assessment of regional left ventricular function. Heart  
 518 92 (8), 1102–8.
- 519 Bellman, R. E., 2003. Dynamic programming. Mineola, N.Y.: Dover Publi-  
 520 cations.
- 521 Belytschko, T., Liu, W., Moran, B., 2001. Nonlinear Finite Elements for  
 522 Continua and Structures. John Wiley & Sons, England.

- 523 Cerqueira, M. D., Weissman, N. J., Dilsizian, V., Jacobs, A. K., Kaul, S.,  
 524 Laskey, W. K., Pennell, D. J., Rumberger, J. A., Ryan, T., Verani, M. S.,  
 525 January 2002. Standardized myocardial segmentation and nomenclature  
 526 for tomographic imaging of the heart: a statement for healthcare pro-  
 527 fessionals from the cardiac imaging committee of the council on clinical  
 528 cardiology of the American Heart Association. *Circulation* 105 (4), 539–  
 529 42.
- 530 Chan, J., Hanekom, L., Wong, C., Leano, R., Cho, G., Marwick, T., Novem-  
 531 ber 2006. Differentiation of subendocardial and transmural infarction using  
 532 two-dimensional strain rate imaging to assess short-axis and long-axis my-  
 533 ocardial function. *J Am Coll Cardiol* 48 (10), 2026–33.
- 534 Chandler, A. G., Pinder, R. J., Netsch, T., Schnabel, J. A., Hawkes, D. J.,  
 535 Hill, D. L. G., Razavi, R., April 2006. Correction of misaligned slices in  
 536 multi-slice MR cardiac examinations by using slice-to-volume registration.  
 537 In: *Third IEEE International Symposium on Biomedical Imaging: From*  
 538 *Nano to Macro, ISBI 2006*. IEEE, Arlington, VA, pp. 474–7.
- 539 Chandrashekara, R., Mohiaddin, R. H., Rueckert, D., October 2004a. Anal-  
 540 ysis of 3D myocardial motion in tagged MR images using non rigid image  
 541 registration. *IEEE Trans Med Imag* 23 (10), 1245–50.
- 542 Chandrashekara, R., Mohiaddin, R. H., Rueckert, D., April 2004b. Cardiac  
 543 motion tracking in tagged MR images using a 4D B-spline motion model  
 544 and nonrigid image registration. In: *IEEE International Symposium on*  
 545 *Biomedical Imaging: From Nano to Macro, ISBI 2004*. IEEE, Arlington,  
 546 VA, USA, pp. 468–71.
- 547 Cover, T. M., Thomas, J. A., 1991. *Elements of information theory*. Wiley-  
 548 Interscience.
- 549 Fischer, S. E., McKinnon, G. C., Maier, S. E., Boesiger, P., August 1993.  
 550 Improved myocardial tagging contrast. *Magnetic Resonance in Medicine*  
 551 30 (2), 191–200.
- 552 Garot, J., Lima, J. A., Gerber, B. L., Sampath, S., Wu, K. C., Bluemke,  
 553 D. A., Prince, J. L., Osman, N. F., November 2004. Spatially resolved  
 554 imaging of myocardial function with strain-encoded MR: comparison with

555 delayed contrast-enhanced MR imaging after myocardial infarction. Radi-  
556 ology 233 (2), 596–602.

557 Geskin, G., Kramer, C. M., Rogers, W. J., Theobald, T. M., Pakstis, D.,  
558 Hu, Y. L., Reichek, N., July 1998. Quantitative assessment of myocar-  
559 dial viability after infarction by dobutamine magnetic resonance tagging.  
560 Circulation 98 (3), 217–23.

561 Hero, A. O., Costa, J., Ma, B., March 2003. Asymptotic relations between  
562 minimal graphs and alpha-entropy. Tech. Rep. CSPL-334, Communica-  
563 tions and Signal Processing Laboratory, The University of Michigan.

564 Ibanez, L., Schroeder, W., Ng, L., Cates, J., 2008. The ITK software guide.  
565 Available at <http://www.itk.org>.

566 Jurcut, R., Pappas, C. J., Masci, P. G., Herbots, L., Szulik, M., Bogaert,  
567 J., Van de Werf, F., Desmet, W., Rademakers, F., Voigt, J. U., D’hooge,  
568 J., August 2008. Detection of regional myocardial dysfunction in patients  
569 with acute myocardial infarction using velocity vector imaging. J Am Soc  
570 Echocardiogr 21 (8), 879–86.

571 Kim, D., Bove, C. M., Kramer, C. M., Epstein, F. H., October 2003. Import-  
572 tance of k-space trajectory in echo-planar myocardial tagging at rest and  
573 during dobutamine stress. Magnetic Resonance in Medicine 50 (4), 813–20.

574 Korosoglou, G., Youssef, A. A., Bilchick, K. C., Ibrahim, E., Lardo, A. C.,  
575 Lai, S., Osman, N. F., May 2008. Real-time fast strain-encoded magnetic  
576 resonance imaging to evaluate regional myocardial function at 3.0 Tesla:  
577 Comparison to conventional tagging. J Magn Reson Imaging 27 (5), 1012–  
578 8.

579 Learned-Miller, E. G., February 2006. Data driven image models through  
580 continuous joint alignment. IEEE Trans. Pattern Anal. Machine Intell.  
581 28 (2), 236–50.

582 Ledesma-Carbayo, M. J., Kybic, J., Desco, M., Santos, A., Suhling, M.,  
583 Hunziker, P., Unser, M., September 2005. Spatio-temporal nonrigid regis-  
584 tration for ultrasound cardiac motion estimation. IEEE Trans Med Imag  
585 24 (9), 1113–26.

- 586 Leonenko, N., Pronzato, L., Savani, V., October 2008. A class of Rényi in-  
587 formation estimators for multidimensional densities. *Annals of Statistics*  
588 36 (5), 2153–82.
- 589 Lilliefors, H., 1967. On the Komogorov-Smirnov test for normality with mean  
590 and variance unknown. *J Am Stat Assoc* 62, 399–402.
- 591 Lorensen, W., Cline, H., July 1987. Marching cubes A high resolution 3D  
592 surface construction algorithm. *Computer Graphics* 4 (21), 163–9.
- 593 Lötjönen, J., Pollari, M., Kivistö, S., Lauerma, K., September 2004. Cor-  
594 rection of movement artifacts from 4D cardiac short and long-axis MR  
595 data. In: Barillot, C., Haynor, D. R., Hellier, P. (Eds.), *Medical Image*  
596 *Computing and Computer-Assisted Intervention – MICCAI 2004*, 7th In-  
597 *ternational Conference, Part II*. Vol. 3217 of *Lecture Notes in Computer*  
598 *Science*. Springer, Saint-Malo, France, pp. 405–12.
- 599 Ma, B., Narayanan, R., Park, H., Hero, A. O., Bland, P. H., Meyer, C. R.,  
600 July 2007. Comparing pairwise and simultaneous joint registrations of  
601 decorrelating interval exams using entropic graphs. In: Karssemeijer, N.,  
602 Lelieveldt, B. P. F. (Eds.), *Information Processing in Medical Imaging*,  
603 *20th International Conference, IPMI 2007*. Vol. 4584 of *Lecture Notes in*  
604 *Computer Science*. Springer, Kerkrade, The Netherlands, pp. 270–82.
- 605 Moore, C. C., Lugo-Olivieri, C. H., McVeigh, E. R., Zerhouni, E. A., Febru-  
606 ary 2000. Three-dimensional systolic strain patterns in the normal human  
607 left ventricle: characterization with tagged MR imaging. *Radiology* 214 (2),  
608 453–66.
- 609 Mount, D. M., August 2006. ANN programming manual. Department of  
610 Computer Science and Institute for Advanced Computer Studies, Univer-  
611 sity of Maryland, College Park, Maryland.
- 612 Neemuchwala, H., Hero, A. O., Zabuawala, S., Carson, P., 2007. Image reg-  
613 istration methods in high-dimensional space. *Int J Imag Syst Tech* 16 (5),  
614 130–45.
- 615 Neemuchwala, H. F., Hero, A. O., 2005. Multi-sensor image fusion and its  
616 applications. Marcel-Dekker, Ch. Entropic graphs for registration, pp. 185–  
617 235.

- 618 Osman, N. F., Kerwin, W. S., McVeigh, E. R., Prince, J. L., 1999. Cardiac  
619 motion tracking using cine harmonic phase (HARP) magnetic resonance  
620 imaging. *Magn Reson Med* 42 (6), 1048–60.
- 621 Pai, V. M., Axel, L., February 2006. Advances in MRI tagging techniques  
622 for determining regional myocardial strain. *Curr Cardiol Rep* 8 (1), 53–8.
- 623 Petitjean, C., Rougon, N., Cluzel, P., April 2005. Assessment of myocadial  
624 function: a review of quantification methods and results using tagged MRI.  
625 *J Cardiovasc Magn Reson* 7 (2), 501–516.
- 626 Petitjean, C., Rougon, N., Prêteux, F., Cluzel, P., Grenier, P., June 2003.  
627 Measuring myocardial deformations from MR data using information-  
628 theoretic non rigid registration. In: Magnin, I. E., Montagnat, J., Clarysse,  
629 P., Nenonen, J., Katila, T. (Eds.), *Functional Imaging and Modeling of  
630 the Heart, Second International Workshop*. Vol. 2674 of *Lecture Notes in  
631 Computer Science*. Springer, Lyon, France, pp. 162–72.
- 632 Petitjean, C., Rougon, N., Prêteux, F., Cluzel, P., Grenier, P., December  
633 2004. Quantification of myocardial function using tagged MR and cine  
634 MR images. *Int J Cardiovasc Imaging* 20 (6), 497–507.
- 635 Quian, Z., Huang, R., Metaxas, D., Axel, L., April 2007. A novel tag removal  
636 technique for tagged cardiac MRI and its applications. In: *Fouth IEEE  
637 International Symposium on Biomedical Imaging: From Nano to Macro,  
638 ISBI 2007*. IEEE, Washington, USA, pp. 364–7.
- 639 Radeva, P., Amini, A., Huang, J., May 1997. Deformable B-solids and im-  
640 plicit snakes for 3D localization and tracking of SPAMM MRI data. *Com-  
641 put Vis Image Understand* 66 (2), 163–78.
- 642 Rao, C., 2002. *Linear Statistical Inference and Its Applications*, 2nd Edition.  
643 Wiley.
- 644 Redmond, C., Yukich, J. E., February 1996. Asymptotics for euclidean func-  
645 tionals with power-weighted edges. *Stochastic Processes and their Appli-  
646 cations* 61 (2), 289–304.
- 647 Rényi, A., June-July 1961. On measures of entropy and information. In: Ney-  
648 man, J. (Ed.), *Proceedings of the Fourth Berkeley Symposium on Math-  
649 ematical Statistics and Probability*. Vol. 1. University of California Press,  
650 Berkeley, CA, USA, pp. 547 – 61.

- 651 Ripley, B. D., January 1996. Pattern Recognition and Neural Networks. Cam-  
652 bridge University Press.
- 653 Rutz, A. K., Ryf, S., Plein, S., Boesiger, P., Kozerke, S., April 2008. Ac-  
654 celerated whole-heart 3D CSPAMM for myocardial motion quantification.  
655 Magn Reson Med 59 (4), 755–63.
- 656 Sabuncu, M. R., Ramadge, P. J., March 2005. Gradient based optimization of  
657 an EMST image registration function. In: IEEE International Conference  
658 on Acoustics, Speech, and Signal Processing. Vol. 2. Philadelphia, PA,  
659 USA, pp. 253–6.
- 660 Sachdev, V., Aletras, A. H., Padmanabhan, S., Sidenko, S., Rao, Y. N.,  
661 Brenneman, C. L., Shizukuda, Y., Lie, G. R., Vincent, P. S., Waclawiw,  
662 M. A., Arai, A. E., January 2006. Myocardial strain decreases with increas-  
663 ing transmuralty of infarction: a Doppler echocardiographic and magnetic  
664 resonance correlation study. J Am Soc Echocardiogr 19 (1), 34–9.
- 665 Schroeder, W., Martin, K., Lorensen, B., 1998. The Visualization Toolkit,  
666 An Object Oriented Approach to 3D Graphics. Kitware Inc.
- 667 Shen, D., Sundar, H., Xue, Z., Fan, Y., Litt, H., October 2005. Consistent  
668 estimation of cardiac motion by 4D image registration. In: Duncan, J. S.,  
669 Gerig, G. (Eds.), Medical Image Computing and Computer-Assisted Inter-  
670 vention – MICCAI 2005, 8th International Conference, Part II. Vol. 3750  
671 of Lecture Notes in Computer Science. Springer, Palm Springs, CA, USA,  
672 pp. 902–10.
- 673 Spottiswoode, B. S., Zhong, X., Hess, A. T., Kramer, C. M., Meintjes, E. M.,  
674 Mayosi, B. M., Epstein, F. H., January 2007. Tracking myocardial motion  
675 from cine DENSE images using spatiotemporal phase unwrapping and tem-  
676 poral fitting. IEEE Trans Med Imag 26 (1), 15–30.
- 677 Sutherland, G. R., Hatle, L., Claus, P., Dhóoge, J., Bijmens, B. H. (Eds.),  
678 2006. Doppler Myocardial Imaging, 1st Edition. BSWK.
- 679 Vartdal, T., Brunvand, H., Pettersen, E., Smith, H. J., Lyseggen, E., Helle-  
680 Valle, T., Skulstad, H., Ihlen, H., Edvardsen, T., April 2007. Early pre-  
681 diction of infarct size by strain Doppler echocardiography after coronary  
682 reperfusion. J Am Coll Cardiol 49 (16), 1715–21.

- 683 Yukich, J. E., 1998. Probability theory of classical Euclidean optimization.  
684 Vol. 1675 of Lecture Notes in Mathematics. Springer-Verlag, Berlin.
- 685 Zerhouni, E., Parish, D., Rogers, W., 1988. Human heart: tagging with MR  
686 imaging - A method for non invasive assessment of myocardial motion.  
687 Radiology 169 (1), 59–63.
- 688 Zhang, Y., Chan, A. K., Yu, C. M., Yip, G. W., Fung, J. W., Lam, W. W., So,  
689 N. M., Wang, M., Wu, E. B., Wong, J. T., Sanderson, J. E., September  
690 2005. Strain rate imaging differentiates transmural from non-transmural  
691 myocardial infarction: a validation study using delayed-enhancement mag-  
692 netic resonance imaging. J Am Coll Cardiol 46 (5), 864–71.